Letter   Editors' Suggestion

Fermi level tuning and double-dome superconductivity in the kagome metal $CsV_3Sb_{5-x}Sn_x$

Yuzki M. Oey [1,*] Brenden R. Ortiz [1], Farnaz Kaboudvand [1], Jonathan Frassineti [2,3] Erick Garcia,[2] Rong Cong,[2]
Samuele Sanna [3], Vesna F. Mitrović [2], Ram Seshadri [1], and Stephen D. Wilson [1,†]

[1]*Materials Department, Materials Research Laboratory, and California NanoSystems Institute,
University of California Santa Barbara, Santa Barbara, California 93106, USA*
[2]*Department of Physics, Brown University, Providence, Rhode Island 02912, USA*
[3]*Department of Physics and Astronomy "A. Righi," University of Bologna, I-40127 Bologna, Italy*

The recently reported AV_3Sb_5 (A = K, Rb, Cs) family of kagome metals are candidates for unconventional superconductivity and chiral charge density wave (CDW) order; both potentially arise from nested saddle points in their band structures close to the Fermi energy. Here, we use chemical substitution to introduce holes into CsV_3Sb_5 and unveil an unconventional coupling of the CDW and superconducting states. Specifically, we generate a phase diagram for $CsV_3Sb_{5-x}Sn_x$ that illustrates the impact of hole doping the system and lifting the nearest van Hove singularity toward and above E_F. Superconductivity exhibits a nonmonotonic evolution with the introduction of holes, resulting in two "domes" peaked at 3.6 and 4.1 K and the rapid suppression of three-dimensional CDW order. The evolution of CDW and superconducting order is compared with the evolution of the electronic band structure of $CsV_3Sb_{5-x}Sn_x$, where the complete suppression of superconductivity seemingly coincides with an electronlike band comprised of Sb p_z orbitals pushed above E_F.

Kagome metals naturally support electronic structures that host Dirac points, flat bands, and saddle points, leading to electronic instabilities associated with divergences in the density of states at the Fermi level. A wide array of instabilities have been predicted, ranging from bond density wave order [1,2] to charge fractionalization [3,4], charge density waves (CDWs) [5], and superconductivity (SC) [1,6]. As a result, the interplay between competing electronic instabilities can often be tuned via small changes in the band filling. For example, band fillings near 5/4 electrons per band [1,7–10] can populate nested van Hove singularities (VHS) that drive CDW order, and, in some limits, unconventional superconductivity.

The recently discovered class of AV_3Sb_5 (A = K, Rb, Cs) kagome metals [11] are potential realizations of this physical mechanism with each member exhibiting experimental signatures associated with CDW order [12–17], followed by the low-temperature onset and coexistence of superconductivity [14,15,18]. Upon applying hydrostatic pressure, the CDW instability in AV_3Sb_5 is coupled to superconductivity in a seemingly unconventional fashion [19,20], and the impact of the pressure-modified band structure on the interplay between the two states remains an open area of study. In particular, understanding the relative roles of the VHS comprised of V d-orbital states near the M points and the electronlike band comprised of Sb states at the Γ point within the CDW and SC mechanisms is essential to developing a microscopic picture of how the two transitions are coupled.

Carrier doping is an appealing means of tuning these features relative to the Fermi level and probing the coupling

of the CDW and SC states. Shifting the relative positions of the VHS and Γ pocket relative to E_F and probing the evolution and interplay of the CDW and SC phase transitions can provide insights into the origins of each state. A recent study on oxidized thin flakes of CsV_3Sb_5, for instance, shows that hole doping on the Cs site can enhance T_C while also suppressing CDW order [21]. In addition, density functional theory (DFT) calculations show that hole doping drives the VHS in the opposite direction relative to E_F than that expected via external hydrostatic pressure [22]. Given that an unusual coupling between SC and CDW states was observed under variable pressure [20], a systematic study of hole-doping effects stands to provide an important experimental window into understanding this unconventional coupling.

Here, the effect of hole doping on the CDW and SC states in $CsV_3Sb_{5-x}Sn_x$ with $0 \leqslant x \leqslant 1.5$ is presented. Hole doping is achieved via substitution of Sn onto the Sb sites, and, because Sn and Sb are very similar in size, this drives negligible coincident steric effects in the band structure. As holes are introduced, the CDW state is rapidly suppressed, and three-dimensional CDW order vanishes near $x = 0.06$. In parallel, SC is enhanced and reaches a maximum $T_C = 3.6$ K at $x = 0.03$ within the CDW state before decreasing as the CDW is fully suppressed. Continued hole doping beyond the suppression of CDW order results in a second maximum in $T_C = 4.1$ K at $x = 0.35$ prior to bulk SC weakening and vanishing beyond $x = 0.5$. DFT calculations and nuclear quadrupolar resonance measurements establish a strong preference for Sn to occupy Sb sites within the kagome plane, and DFT models predict that Sn substitution on this site lifts the Sb p_z electronlike band at Γ above E_F coincident with the vanishing of bulk SC. Furthermore, only small changes in the energies of the VHS are predicted for doping levels

*yoey@ucsb.edu
†stephendwilson@ucsb.edu

sufficient to suppress signatures of CDW order, suggesting the importance of Sb states in the stabilization of both phases.

Powder samples of $CsV_3Sb_{5-x}Sn_x$ for $0 \leqslant x \leqslant 1$ in 6–7 g batches were synthesized using a combination of ball milling and high-temperature sintering [23]. A structural analysis was performed via synchrotron powder x-ray data acquired at Argonne National Laboratory (APS, 11-BM) and on a Panalytical Empyrean laboratory x-ray powder diffractometer. A Hitachi TM4000Plus scanning electron microscope (SEM) was used to perform energy-dispersive x-ray spectroscopy (EDS). Magnetization data were collected in a Quantum Design magnetic property measurement system (MPMS) and electrical resistivity data were collected in a Quantum Design physical property measurement system (PPMS). DFT calculations were performed within the Vienna *ab initio* simulation package (VASP) [24,25], and room-temperature ^{121}Sb zero-field nuclear quadrupole resonance (NQR) measurements were performed using a custom NMR spectrometer. Further details are available in the Supplemental Material [23], which includes Refs. [26–34].

At room temperature, $CsV_3Sb_{5-x}Sn_x$ with $0 \leqslant x \leqslant 1$ all adopt the same hexagonal $P6/mmm$ structure as CsV_3Sb_5 with an ideal kagome network of V atoms, shown in Fig. 1(a). For $0 \leqslant x \leqslant 1$, polycrystalline samples were found to be single phase, while a secondary phase appears for $x = 1.5$, indicating the termination of the solid solution. Pawley fits of powder diffraction data were used to determine changes to the unit cell as a function of Sn content. Figures 1(b) and 1(c) show the normalized c/a ratio and the cell volume as a function of Sn content. With increasing Sn, a increases and c decreases in near perfect compensation, yielding a cell volume which is virtually independent of Sn content. Small fluctuations in volume of less than 0.16% can be explained by uncertainties in chemical composition and in the structural refinement.

The linear trend in c/a is reminiscent of a Vegard's law-type trend, suggesting that Sn is incorporated into the parent structure as a solid solution up to approximately $x = 1$, at which point the c/a ratio plateaus. Figure 1(d) indicates that the measured Sn content (via EDS) tracks the nominal Sn content. While Rietveld refinements of x-ray data confirm that powders are single phase, poor scattering contrast between Sb and Sn impedes the ability to refine whether Sn is uniformly distributed on both the Sb1 and Sb2 sites, or whether there is preferential occupation of a particular sublattice. DFT calculations suggest a preference ≈ 10 meV/atom for Sn to substitute preferentially on the Sb1 (in the kagome plane) and NQR measurements (discussed later) confirm that Sn atoms preferentially occupy this site [23].

Undoped CsV_3Sb_5 single crystals have a superconducting $T_C = 2.5$ K [14,21] and a charge density wave transition temperature $T^* = 94$ K [13,16] that drives a structural distortion into a $2 \times 2 \times 4$ enlarged unit cell, one containing layers of kagome nets distorted into both star-of-David and trihexagonal structures [13,35,36]. Polycrystalline samples show identical transition temperatures, although both transitions are broader compared to single crystals [14]. This is largely due to powders being very sensitive to exact synthesis conditions and strain effects [23]. Pure CsV_3Sb_5 powder synthesized here has an onset T_C of 2.70 K and a midpoint
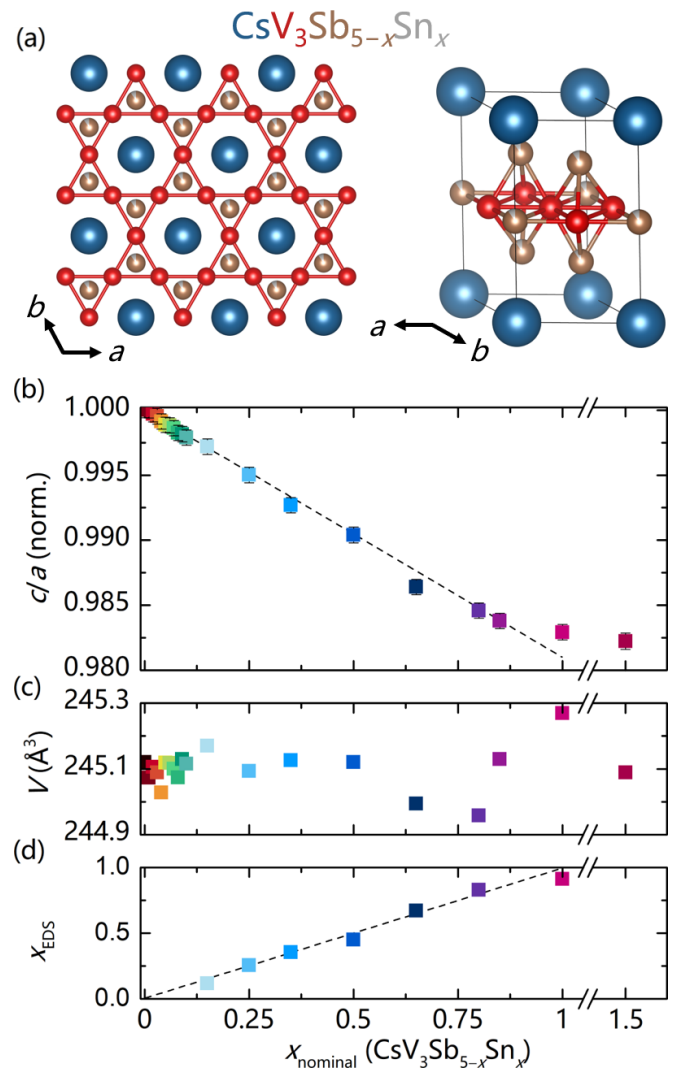

FIG. 1. (a) $CsV_3Sb_{5-x}Sn_x$ crystallizes in the parent CsV_3Sb_5 ($P6/mmm$) structure. Sn can substitute on either the Sb1 or Sb2 sublattices, and at low doping we establish a preference for the Sb site in the V kagome plane. (b), (c) Sn integration into $CsV_3Sb_{5-x}Sn_x$ causes the c/a ratio to steadily decrease until the termination of solid solubility at $x = 1$. (d) For samples with concentrations above EDS sensitivity threshold, nominal Sn tracks measured Sn. Error bars are shown unless they are smaller than the associated point size. The different colors correspond to sample composition and are consistent throughout the figures.

T_C of 2.07 K. As Sn is added within the matrix, Fig. 2(a) shows the evolution of superconductivity, focusing on two different doping regimes ($x = 0$–0.03 and $x = 0.1$–0.35). All superconducting samples show $4\pi \chi_v \approx -1$ in magnetization. Fractions slightly exceeding unity are attributed to errors in the packing density, and data are normalized to -1 for ease of comparison. The effect of Sn on T_C becomes immediately apparent: As the Sn content is increased to $x = 0.03$, T_C increases to a local maxima of 3.6 K. T_C then decreases with continued hole doping, followed by a second superconducting dome appearing shortly thereafter with a maximum $T_C = 4.1$ K at $x = 0.35$. Superconductivity assumes only a partial volume fraction for $x > 0.5$, and the SC state completely
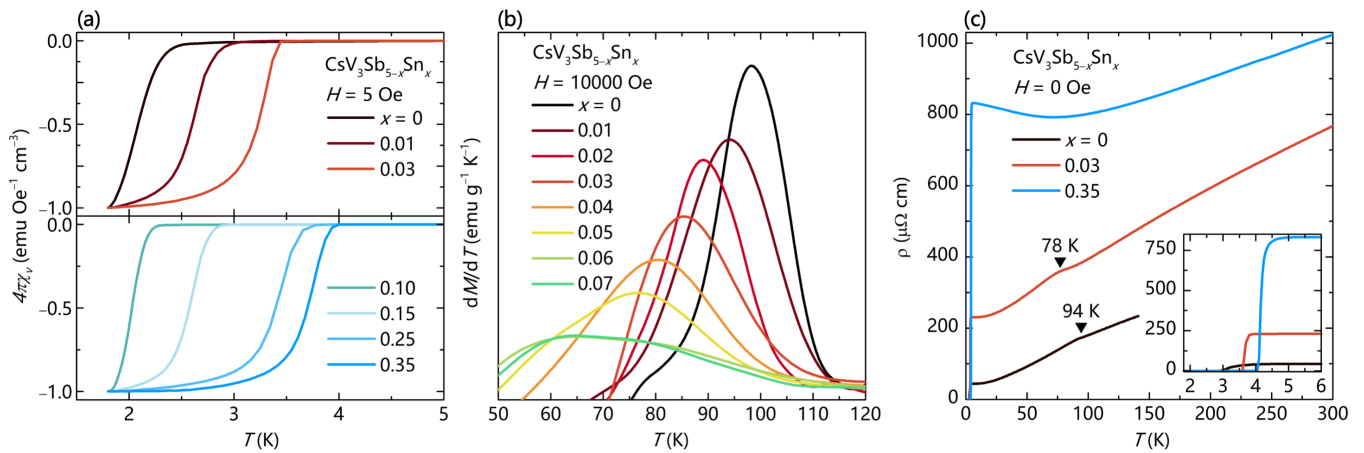
FIG. 2. (a) The superconducting T_C measured under a field of $H = 5$ Oe shows a systematic shift to higher temperature in the compositions leading to the two T_C maximums. The superconducting fraction is normalized to account for errors in mass and packing fraction so all data have a minimum of -1, the theoretical minimum. (b) dM/dT for compositions $x \leqslant 0.06$ show a decrease in CDW T^*, and this transition disappears for greater Sn compositions. (c) Resistivity data also show this enhancement in T_C, and the low-T, normal-state resistivity for $x = 0.35$ is about four times higher than $x = 0.03$.

disappears by $x = 0.85$. An exhaustive set of susceptibility measurements is provided in the Supplemental Material [23].

The evolution of CDW order upon hole doping can be monitored via the inflection point in magnetization that appears at the CDW onset. Using the peak in dM/dT as a metric for the onset of three-dimensional CDW order, Fig. 2(b) shows that light hole substitution causes the CDW transition to rapidly broaden and shift to lower temperatures. Undoped, the peak in dM/dT is 98.01 K and this peak decreases to less than 80 K at $x = 0.04$. For $x > 0.05$, signatures of the CDW transition in magnetization cannot be resolved, although it is possible that a highly broadened CDW anomaly smoothly continues its rapid suppression with higher Sn doping. Despite the ambiguity in the precise position of CDW phase boundary near $x = 0.05$, the superconducting and CDW states clearly coexist at the first maximum of the first superconducting dome ($x = 0.03$). This is distinct from the second maximum in T_C at higher Sn content ($x = 0.35$), which occurs far beyond the apparent suppression of CDW order. Future work studying single crystals will be required to fully map if the suppression of the CDW state is a first- or second-order phase boundary and to fully explore whether CDW order is becoming short ranged at larger Sn-doping levels.

Figure 2(c) shows electrical resistivity measurements performed on samples at both peak T_C values ($x = 0.03$ and $x = 0.35$). Zero-resistivity conditions agree well with the T_C obtained via magnetization measurements, and the CDW onset temperature is further marked for the sample with $x = 0.03$. The resistance immediately prior to the onset of SC increases quite dramatically upon Sn substitution, from 50 $\mu\Omega$ cm ($x = 0$), to 250 $\mu\Omega$ cm ($x = 0.03$, first T_C peak), to 800 $\mu\Omega$ cm ($x = 0.35$, second T_C peak), and the temperature dependence of the resistivity, particularly near the CDW temperature, changes dramatically with Sn doping. As a summary, Fig. 3 plots a phase diagram showing the effect of Sn substitution on both SC and CDW orders. A two-dome structure is immediately evident in T_C, as is the relatively rapid suppression of CDW order with the introduction of Sn.

The CsV_3Sb_5 lattice supports nearly 1/5 of the total Sb being replaced by Sn. To give a rough sense of the range over which E_F can be tuned, Fig. 4(a) shows the electronic structure of pure CsV_3Sb_5 along with the range of Fermi levels achievable with a loss of 1 electron per unit cell (gray-shaded region). In a rigid-band shift approximation, substitution of Sn should allow E_F to be tuned across multiple VHS and
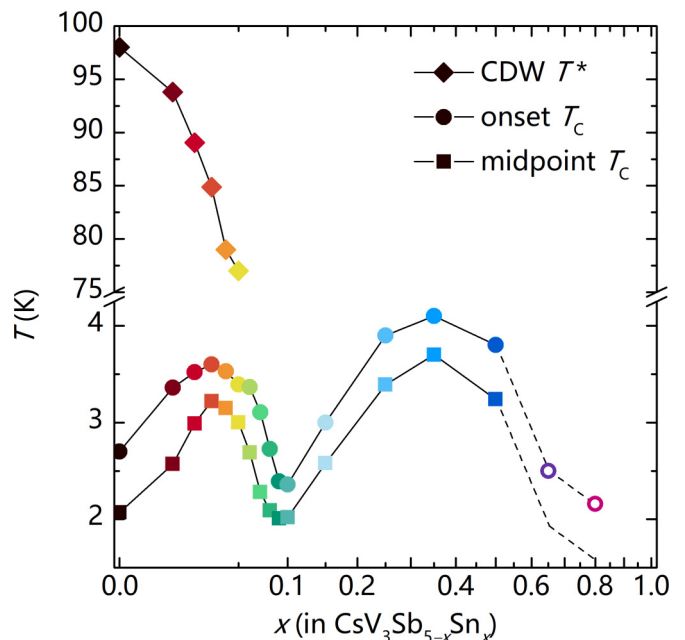

FIG. 3. Hole-doping phase diagram for $CsV_3Sb_{5-x}Sn_x$. The double-dome structure is clearly evident, as is the depression of the CDW ordering temperature. T_C shows two maxima at $x = 0.03$ and at $x = 0.35$ and the CDW state disappears by $x = 0.06$. We note that the first T_C maximum occurs while the CDW is still present, and the CDW vanishes once T_C is already declining again $x > 0.03$. For $x \geqslant 0.65$, the volume fraction of superconductivity decreases and the onset T_C's are represented with open circles.
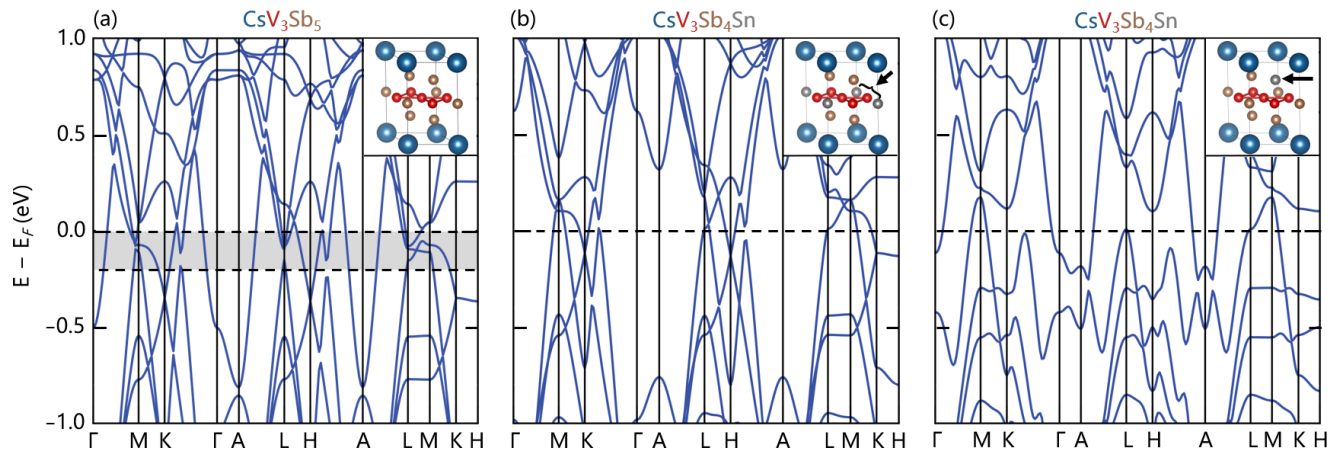
FIG. 4. (a) DFT calculations for CsV_3Sb_5 highlighting the allowable range of Fermi levels under the rigid-band approximation for substitution of one Sn atom per formula unit. (b) Calculation of the band structure of CsV_3Sb_4Sn where one Sn has been substituted within the kagome plane. Here, the majority of the electronic structure is preserved with the exception of the Γ pocket, where the occupied Sb band is replaced with an unoccupied Sn band above E_F. (c) Calculation of the band structure of CsV_3Sb_4Sn where one Sn has been substituted at a Sb site outside of the kagome plane (OKP). A strong reconstruction of many bands can be observed, in particular near K, H, and K-Γ.

Dirac points near the M and K points, respectively. However, reconstruction of the bands associated with the Sb orbitals and orbital-selective doping effects are expected, and Fig. 4(c) shows one hypothetical structure with Sn substituted on the Sb2 sublattice (out of the kagome plane). Here, in addition to the expected shift of the Fermi level (note the position of the M-point VHS crossing now $\approx$0.2 eV *above* E_F), a significant reconstruction is also resolved around the K, L, and H points. Notably, the electronlike band at Γ is preserved in this $x = 1$ structure. Alternatively, if Sn substitution instead occupies the Sb1 sublattice within the kagome plane, the overall electronic structure relative to CsV_3Sb_5 is largely preserved and mimics a rigid-band shift model, with the important exception of the Sb-derived Γ pocket, which vanishes and is replaced with an electronlike Sn band far above E_F. Colorized orbital contributions to the band-structure structures shown in Fig. 4 are presented in the Supplemental Material [23].

To clarify the impact of Sn doping on the band structure, NQR measurements were performed and establish that Sn preferentially occupies the Sb1 sites in the kagome plane [23]. This is consistent with DFT calculations that show a small energy preference for Sn occupying the Sb1 site. With this doping site established, supercell calculations at fractional in-plane Sb substitution were performed and show that, as Sn content is increased, the electronlike band at Γ lifts above E_F near $x = 0.5$, in tandem with the disappearance of bulk superconductivity [23]. This suggests that superconductivity in CsV_3Sb_5 in part relies on the Sb p_z-derived orbitals, and aligns with results of earlier pressure studies [37].

At smaller Sn-doping levels, the observation of an intermediate peak in T_C demonstrates a complex interplay between the Sb states at Γ and the V d states driving the CDW order. Supercell calculations show a rather mild shift in the M-point VHS from roughly -0.072 eV below E_F for $x = 0$ to -0.047 eV for $x = 0.33$ and -0.042 eV for $x = 0.5$, prior to shifting 0.083 eV above E_F in $x = 1$. The small shift in the expected energies of the VHS toward E_F under mild $x = 0.05$ substitution fails to explain the rapid suppression of the CDW

state at this doping, suggesting a complicated balance of energy scales underpinning the CDW state. This is consistent with the rapid suppression of the CDW state under hydrostatic pressure [19,20]; however, the two SC domes apparent under hole doping seem distinct from those realized under pressure. Superconductivity in crystals nominally doped between the SC domes retains a sharp transition [23], unlike the weak SC observed in pressure studies. Further work exploring the distinctions between pressure (pushing VHS away from E_F) and hole doping (pulling VHS toward E_F) is required to fully explore the parallels between the hole doping and pressure-driven phase diagrams.

Hole doping realized via chemical substitution of Sn into CsV_3Sb_5 results in a complex electronic phase diagram featuring two SC domes—one that coexists with CDW order and a second that appears following the suppression of the CDW state. Unconventional superconductivity has been predicted for fillings slightly away from the VHS [8]. The peak in T_C prior to the suppression of CDW order and the subsequent, second peak in T_C following the complete suppression of the CDW state motivates deeper theoretical studies into how the Sb p_z states intertwine with both CDW order SC in these materials. Our results demonstrate that small changes in the electronic structure achieved through carrier doping can have dramatic impacts on SC and CDW orders in CsV_3Sb_5 and provide a elegant chemical means to tune the competition between these states in the AV_3Sb_5 class of kagome superconductors.

[1] W.-S. Wang, Z.-Z. Li, Y.-Y. Xiang, and Q.-H. Wang, Competing electronic orders on kagome lattices at van Hove filling, Phys. Rev. B **87**, 115135 (2013).

[2] S. V. Isakov, S. Wessel, R. G. Melko, K. Sengupta, and Y. B. Kim, Hard-Core Bosons on the Kagome Lattice: Valence-Bond Solids and their Quantum Melting, Phys. Rev. Lett. **97**, 147202 (2006).

[3] A. O'Brien, F. Pollmann, and P. Fulde, Strongly correlated fermions on a kagome lattice, Phys. Rev. B **81**, 235115 (2010).

[4] A. Rüegg and G. A. Fiete, Fractionally charged topological point defects on the kagome lattice, Phys. Rev. B **83**, 165118 (2011).

[5] H.-M. Guo and M. Franz, Topological insulator on the kagome lattice, Phys. Rev. B **80**, 113102 (2009).

[6] W.-H. Ko, P. A. Lee, and X.-G. Wen, Doped kagome system as exotic superconductor, Phys. Rev. B **79**, 214502 (2009).

[7] S.-L. Yu and J.-X. Li, Chiral superconducting phase and chiral spin-density-wave phase in a Hubbard model on the kagome lattice, Phys. Rev. B **85**, 144402 (2012).

[8] M. L. Kiesel, C. Platt, and R. Thomale, Unconventional Fermi Surface Instabilities in the Kagome Hubbard Model, Phys. Rev. Lett. **110**, 126405 (2013).

[9] K. Barros, J. W. F. Venderbos, G.-W. Chern, and C. D. Batista, Exotic magnetic orderings in the kagome Kondo-lattice model, Phys. Rev. B **90**, 245119 (2014).

[10] X. Feng, K. Jiang, Z. Wang, and J. Hu, Chiral flux phase in the Kagome superconductor AV$_3$Sb$_5$, Sci. Bull. **66**, 1384 (2021).

[11] B. R. Ortiz, L. C. Gomes, J. R. Morey, M. Winiarski, M. Bordelon, J. S. Mangum, I. W. H. Oswald, J. A. Rodriguez-Rivera, J. R. Neilson, S. D. Wilson *et al.*, New kagome prototype materials: Discovery of KV$_3$Sb$_5$, RbV$_3$Sb$_5$, and CsV$_3$Sb$_5$, Phys. Rev. Materials **3**, 094407 (2019).

[12] Y.-X. Jiang, J.-X. Yin, M. M. Denner, N. Shumiya, B. R. Ortiz, G. Xu, Z. Guguchia, J. He, M. S. Hossain, X. Liu *et al.*, Unconventional chiral charge order in kagome superconductor KV$_3$Sb$_5$, Nat. Mater. **20**, 1353 (2021).

[13] H. Zhao, H. Li, B. R. Ortiz, S. M. Teicher, T. Park, M. Ye, Z. Wang, L. Balents, S. D. Wilson, and I. Zeljkovic, Cascade of correlated electron states in a kagome superconductor CsV$_3$Sb$_5$, Nature (London) **599**, 216 (2021).

[14] B. R. Ortiz, S. M. L. Teicher, Y. Hu, J. L. Zuo, P. M. Sarte, E. C. Schueller, A. M. M. Abeykoon, M. J. Krogstad, S. Rosenkranz, R. Osborn, R. Seshadri, L. Balents, J. He, and S. D. Wilson, CsV$_3$Sb$_5$: A $\mathbb{Z}_2$ Topological Kagome Metal with a Superconducting Ground State, Phys. Rev, Lett. **125**, 247002 (2020).

[15] B. R. Ortiz, P. M. Sarte, E. M. Kenney, M. J. Graf, S. M. L. Teicher, R. Seshadri, and S. D. Wilson, Superconductivity in the $\mathbb{Z}_2$ kagome metal KV$_3$Sb$_5$, Phys. Rev. Materials **5**, 034801 (2021).

[16] Z. Liang, X. Hou, W. Ma, F. Zhang, P. Wu, Z. Zhang, F. Yu, J.-J. Ying, K. Jiang, L. Shan *et al.*, Three-Dimensional Charge Density Wave and Robust Zero-Bias Conductance Peak Inside the Superconducting Vortex Core of a Kagome Superconductor CsV$_3$Sb$_5$, Phys. Rev. X **11**, 031026 (2021).

[17] H. Chen, H. Yang, B. Hu, Z. Zhao, J. Yuan, Y. Xing, G. Qian, Z. Huang, G. Li, Y. Ye *et al.*, Roton pair density wave in a strong-coupling kagome superconductor, Nature (London) **599**, 222 (2021).

[18] Q. Yin, Z. Tu, C. Gong, Y. Fu, S. Yan, and H. Lei, Superconductivity and normal-state properties of kagome metal RbV$_3$Sb$_5$ single crystals, Chin. Phys. Lett. **38**, 037403 (2021).

[19] F. Du, S. Luo, B. R. Ortiz, Y. Chen, W. Duan, D. Zhang, X. Lu, S. D. Wilson, Y. Song, and H. Yuan, Pressure-induced double superconducting domes and charge instability in the kagome metal KV$_3$Sb$_5$, Phys. Rev. B **103**, L220504 (2021).

[20] K. Y. Chen, N. N. Wang, Q. W. Yin, Y. H. Gu, K. Jiang, Z. J. Tu, C. S. Gong, Y. Uwatoko, J. P. Sun, H. C. Lei *et al.*, Double Superconducting Dome and Triple Enhancement of T_C in the Kagome Superconductor CsV$_3$Sb$_5$ under High Pressure, Phys. Rev. Lett. **126**, 247001 (2021).

[21] Y. Song, T. Ying, X. Chen, X. Han, X. Wu, A. P. Schnyder, Y. Huang, J. Guo, and X. Chen, Competition of Superconductivity and Charge Density Wave in Selective Oxidized CsV$_3$Sb$_5$ Thin Flakes, Phys. Rev. Lett. **127**, 237001 (2021).

[22] H. LaBollita and A. S. Botana, Tuning the van Hove singularities in AV$_3$Sb$_5$ (A= K, Rb, Cs) via pressure and doping, Phys. Rev. B **104**, 205129 (2021).

[23] See Supplemental Material at http://link.aps.org/supplemental/10.1103/PhysRevMaterials.6.L041801 for more detailed information regarding synthesis and characterization of the materials presented in the main text.

[24] G. Kresse and J. Furthmüller, Efficient iterative schemes for *ab initio* total-energy calculations using a plane-wave basis set, Phys. Rev. B **54**, 11169 (1996).

[25] G. Kresse and J. Furthmüller, Efficiency of ab-initio total energy calculations for metals and semiconductors using a plane-wave basis set, Comput. Mater. Sci. **6**, 15 (1996).

[26] A. A. Coelho, TOPAS and TOPAS-Academic: An optimization program integrating computer algebra and crystallographic objects written in C++, J. Appl. Crystallogr. **51**, 210 (2018).

[27] G. W. Stinton and J. S. Evans, Parametric Rietveld refinement, J. Appl. Crystallogr. **40**, 87 (2007).

[28] K. Momma and F. Izumi, VESTA 3 for three-dimensional visualization of crystal, volumetric and morphology data, J. Appl. Crystallogr. **44**, 1272 (2011).

[29] A. Abragam, *The Principles of Nuclear Magnetism*, International Series of Monographs on Physics Vol. 32 (Oxford University Press, Oxford, UK, 1961).

[30] P. E. Blöchl, Projector augmented-wave method, Phys. Rev. B **50**, 17953 (1994).

[31] G. Kresse and D. Joubert, From ultrasoft pseudopotentials to the projector augmented-wave method, Phys. Rev. B **59**, 1758 (1999).

[32] W. Setyawan and S. Curtarolo, High-throughput electronic band structure calculations: Challenges and tools, Comput. Mater. Sci. **49**, 299 (2010).

[33] A. M. Ganose, A. J. Jackson, and D. O. Scanlon, Sumo: Command-line tools for plotting and analysis of periodic *ab initio* calculations, J. Open Source Softw. **3**, 717 (2018).

[34] J. Luo, Z. Zhao, Y. Z. Zhou, J. Yang, A. F. Fang, H. T. Yang, H. J. Gao, R. Zhou, and G. Zheng, Possible star-of-David pattern charge density wave with additional modulation in the kagome superconductor CsV_3Sb_5, npj Quantum Mater. **7**, 30 (2022).

[35] B. R. Ortiz, S. M. L. Teicher, L. Kautzsch, P. M. Sarte, N. Ratcliff, J. Harter, J. P. C. Ruff, R. Seshadri, and S. D. Wilson, Fermi Surface Mapping and the Nature of Charge-Density-Wave Order in the Kagome Superconductor CsV_3Sb_5, Phys. Rev. X **11**, 041030 (2021).

[36] Y. Hu, X. Wu, B. R. Ortiz, X. Han, N. C. Plumb, S. D. Wilson, A. P. Schnyder, and M. Shi, Coexistence of tri-hexagonal and star-of-David pattern in the charge density wave of the kagome superconductor AV_3Sb_5, arXiv:2201.06477.

[37] A. A. Tsirlin, P. Fertey, B. R. Ortiz, B. Klis, V. Merkl, M. Dressel, S. D. Wilson, and E. Uykur, Anisotropic compression and role of Sb in the superconducting kagome metal CsV_3Sb_5, SciPost Phys. **12**, 049 (2022).

[38] www.mrfn.org.